Magnetic-Based Motion Control of Paramagnetic Microparticles with Disturbance Compensation

Islam S. M. Khalil*, Leon Abelmann† and Sarthak Misra‡

Magnetic systems have the potential to control the motion of microparticles and microrobots during targeted drug delivery. During their manipulation, a nominal magnetic force-current map is usually derived and used as a basis of the control system design. However, the inevitable mismatch between the nominal and actual force-current maps along with external disturbances affect the positioning accuracy of the motion control system. In this work, we devise a control system which allows for the realization of the nominal magnetic force-current map and the point-to-point positioning of paramagnetic microparticles. This control is accomplished by estimating and rejecting the two-dimensional disturbance forces using an inner-loop based on a disturbance force observer. In addition, an outer-loop is utilized to achieve stable dynamics of the overall magnetic system. The control system is implemented on a magnetic system for controlling microparticles of paramagnetic material, which experience magnetic forces that are related to the gradient of the field-squared. We evaluate the performance of our control system by analyzing the transient- and steady-state characteristics of the controlled microparticle for two cases. The first case is done without estimating and rejecting the mismatch and the disturbance forces, whereas the second case is done while compensating for these disturbance forces. We do not only obtain 17% faster response during the transient-state, but we are also able to achieve 23% higher positioning accuracy in the steady-state for the second case (compensating disturbance forces). Although the focus of this paper is on the wireless magnetic-based control of paramagnetic microparticle, the presented control system is general and can be adapted to control microrobots.

***Index Terms*—Wireless, magnetic, micromanipulation, model mismatch, disturbance force observer, disturbance compensation.**

I. Introduction

PARAMAGNETIC microparticles and nanoparticles have the potential to perform localized drug delivery by selectively targeting diseased tissue [1]-[6]. These particles are steered under the influence of the applied magnetic fields. In manipulating these particles, a magnetic force-current map has to be determined and used as a basis of the control system design [7], [8]. Derivation of the correct force-current map is not simple since weak magnetic field (less than 3 mT) results in constant susceptibility and permeability, whereas stronger magnetic fields do not guarantee the same result [9]. The most often cited force-current map under weak magnetic field is proven not to match the experimental data due to the absence of the initial magnetization [10]. However, accounting for the non-zero initial magnetization corrects the expression of the magnetic force experienced by microparticles under the influence of weak magnetic fields.

Some researchers preferred the utilization of spherical microparticles (Fig. 1) since the direction of magnetization does not have to be specified [11]-[15]. Microparticles with irregular shapes under uniform applied fields have magnetization force which differs throughout their bodies in an unknown manner. This irregularity has a disadvantage for microparticles or microrobots whose surface is not of second degree (ellipsoid has surface with second degree) [16], [17]. Material also affects the relation between the applied field and the magnetization of the microparticle. Microparticles with soft-magnetic material for instance have non-linear relation between the applied magnetic field and the magnetization.

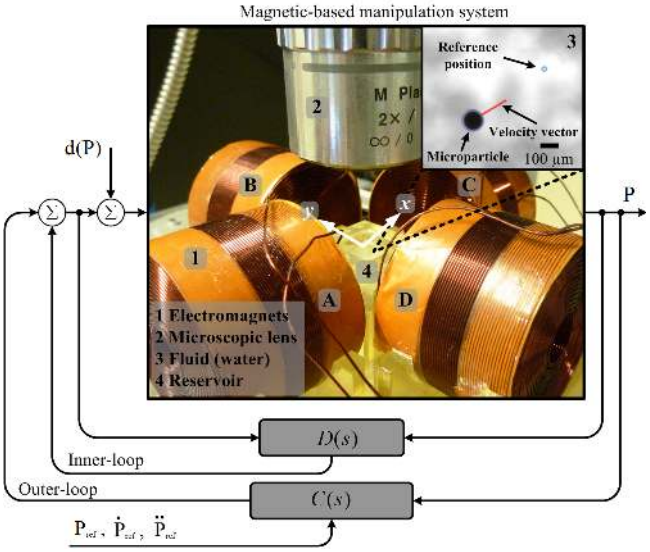

Fig. 1. Magnetic-based manipulation system with inner- and outer-loops: The input disturbance force ($\mathbf{d}(\mathbf{P})$) represents the model mismatch and external disturbance forces on the system. The output of the disturbance force observer ($D(s)$) compensates for the model mismatch and the external disturbances, whereas the output of the control system ($C(s)$) stabilizes the overall dynamics of the system. The inset shows a 100 μm spherical paramagnetic microparticle moving towards a reference position (small blue circle) under the influence of the applied magnetic fields. The large blue circle indicates the microparticle and is assigned by our feature tracking software [12]. The red line represents the velocity vector of the microparticle. The actual and reference position vectors are represented by $\mathbf{P}$ and $\mathbf{P}_{\mathrm{ref}}$, respectively. The electromagnets are labeled with the letters A, B, C and D.

Designing a microparticle or a microrobot to be satisfactory under all conditions is almost impossible. Fabrication of soft-magnetic microparticles for instance is relatively easy.

*Islam S. M. Khalil was affiliated with MIRA–Institute for Biomedical Technology and Technical Medicine, University of Twente, The Netherlands. He is now affiliated with the German University in Cairo, Egypt (islam.shoukry@guc.edu.eg).

†Leon Abelmann is affiliated with MESA+ Institute for Nanotechnology, University of Twente, The Netherlands. He is also affiliated with the Korean Institute of Science and Technology, Germany (l.abelmann@utwente.nl).

‡Sarthak Misra is affiliated with MIRA–Institute for Biomedical Technology and Technical Medicine, University of Twente, The Netherlands (s.misra@utwente.nl).

However, its magnetization is non-linearly proportional to the applied magnetic fields. Therefore, the governing equations relating the applied magnetic field and the magnetization (or the resulting magnetic force and torque) are not accurate. It would be natural to devise control systems with relatively large stability margins to tolerate the model mismatch and the dynamical uncertainties.

This work is concerned with the design of a control system for magnetically-guided paramagnetic microparticles. First the governing equation in terms of magnetic force-current map is derived. This equation depends on the field-current map of our magnetic system, shown in Fig. 1. We model this map using finite element (FE) analysis, then this model is verified by measuring the actual fields within the workspace of our magnetic system. This verification results in an inevitable mismatch for the field-current map, which in turn results in a mismatch for the force-current map. The mismatch between the governing equation and the actual system along with the external disturbances and drag forces are modeled as an input disturbance force to the governing motion equation of the paramagnetic microparticle. An inner-loop is devised to estimate this disturbance force and convert it into a compensating control input [18], [19]. This inner-loop compensates only for the disturbance forces along x- and y-axis, since our magnetic system is designed for the manipulation of microparticles in a two-dimensional workspace. In addition, an outer-loop is devised to achieve stability of the overall magnetic system based on specific transient- and steady-state characteristics. The experimental work provided in this paper is performed on a magnetic system which has a similar configuration to the lower set of OctoMag [7]. The merits and novelty of our work are due to the design of a closed-loop control system for microparticles of paramagnetic material. This system allows for the point-to-point positioning of these microparticles and the simultaneous rejection of the disturbance forces.

The remainder of this paper is organized as follows: In Section II, we discuss the theoretical background pertaining to the modeling of paramagnetic microparticles under the influence of external magnetic fields. Section III provides the model mismatch and disturbance estimation analysis, and the design of a disturbance force observer [20]. In Section IV, a motion control strategy is presented, based on the estimation and compensation of the disturbance force using an inner-loop, along with achieving stability of the magnetic system using an outer-loop. Description of the magnetic system and the experimental results are provided in Section V. Finally, discussion about the presented control strategy, conclusions and future work are provided in Section VI.

II. Magnetic Force Modeling

The planar magnetic force ($\mathbf{F}(\mathbf{P}) \in \mathbb{R}^{2\times 1}$) acting on a magnetic dipole is given by

$$\mathbf{F}(\mathbf{P}) = \nabla(\mathbf{m}(\mathbf{P}) \cdot \mathbf{B}(\mathbf{P})), \tag{1}$$

where $\mathbf{m}(\mathbf{P}) \in \mathbb{R}^{2\times 1}$ and $\mathbf{B}(\mathbf{P}) \in \mathbb{R}^{2\times 1}$ are the permanent or induced magnetic dipole moment of the microparticle and the induced magnetic field at point ($\mathbf{P} \in \mathbb{R}^{2\times 1}$), respectively [21], [22]. The microparticles we consider in this work have spherical geometry. Therefore, their induced magnetic dipole moment can be determined as the volume integral of the induced magnetization ($\mathbf{M}(\mathbf{P})$) [23]

$$\mathbf{m}(\mathbf{P}) = \int_V \mathbf{M}(\mathbf{P}) \mathrm{d}V = \frac{4}{3}\pi r_{\mathrm{p}}^3 \mathbf{M}(\mathbf{P}), \tag{2}$$

where V and r_{p} are the volume and radius of the spherical microparticle, respectively. The induced magnetization is related to the magnetic field strength ($\mathbf{H}(\mathbf{P})$) by $\mathbf{M}(\mathbf{P}) = \chi_{\mathrm{m}}\mathbf{H}(\mathbf{P})$, where χ_{m} is the magnetic susceptibility constant [24]. The induced magnetization vector ($\mathbf{M}(\mathbf{P})$) always aligns itself with the applied field since there is no shape anisotropy for the spherical microparticles. This observation simplifies the model as the microparticles will be subjected to pure force and zero magnetic torque. However, the control system we consider in this work is fairly general and can be implemented on non-spherical microparticles which experience magnetic force and torque. Rewriting (2) as

$$\mathbf{m}(\mathbf{P}) = \frac{4}{3}\pi r_{\mathrm{p}}^3 \chi_{\mathrm{m}} \mathbf{H}(\mathbf{P}) = \frac{1}{\mu}\frac{4}{3}\pi r_{\mathrm{p}}^3 \chi_{\mathrm{m}} \mathbf{B}(\mathbf{P}), \tag{3}$$

where μ is the permeability coefficient given by, $\mu = \mu_0(1 + \chi_{\mathrm{m}})$, and $\mathbf{B}(\mathbf{P}) = \mu\mathbf{H}(\mathbf{P})$. Further, μ_0 is the permeability of vacuum ($\mu_0 = 4\pi \times 10^{-7}\mathrm{T.m/A}$). Substitution of (3) in (1) yields

$$\mathbf{F}(\mathbf{P}) = \frac{4}{3}\frac{1}{\mu}\pi r_{\mathrm{p}}^3 \chi_{\mathrm{m}} \nabla \left(\mathbf{B}^{\mathrm{T}}(\mathbf{P})\mathbf{B}(\mathbf{P})\right). \tag{4}$$

In this work, the magnetic field is generated using air-core electromagnets, and does not allow the microparticles to reach saturation. Therefore, the magnetic field can be determined by the superposition of the contribution of each of the electromagnets [7]

$$\mathbf{B}(\mathbf{P}) = \sum_{i=1}^{e} \mathbf{B}_i(\mathbf{P}), \tag{5}$$

where e is the number of electromagnets within the magnetic system. The magnetic field ($\mathbf{B}_i(\mathbf{P})$) is linearly proportional to the applied current (I_i) at the ith electromagnet. Therefore, (5) can be rewritten as

$$\mathbf{B}(\mathbf{P}) = \sum_{i=1}^{e} \widetilde{\mathbf{B}}_i(\mathbf{P}) I_i = \widetilde{\mathbf{B}}(\mathbf{P})\mathbf{I}, \tag{6}$$

where $\widetilde{\mathbf{B}}(\mathbf{P}) \in \mathbb{R}^{2\times e}$ is a matrix which depends on the position at which the magnetic field is evaluated and $\mathbf{I} \in \mathbb{R}^{e\times 1}$ is a vector of the applied current. The magnetic field due to each electromagnet is related to the current input by $\widetilde{\mathbf{B}}_i(\mathbf{P})$.

The FE analysis of the field-current map (6) is provided in Fig. 2. This map has to be constructed to determine the gradient of the magnetic field-squared ($\nabla(\mathbf{B}^{\mathrm{T}}(\mathbf{P})\mathbf{B}(\mathbf{P}))$), which is used in the determination of the magnetic force-field map (4). The FE model is developed for a magnetic system with four orthogonally-oriented air-core electromagnets. As shown in Fig. 2, the FE model provides the magnetic fields, the field-squared and the gradients of the field-squared in a workspace of 40 $\times$ 40 mm^2 within the center of our magnetic

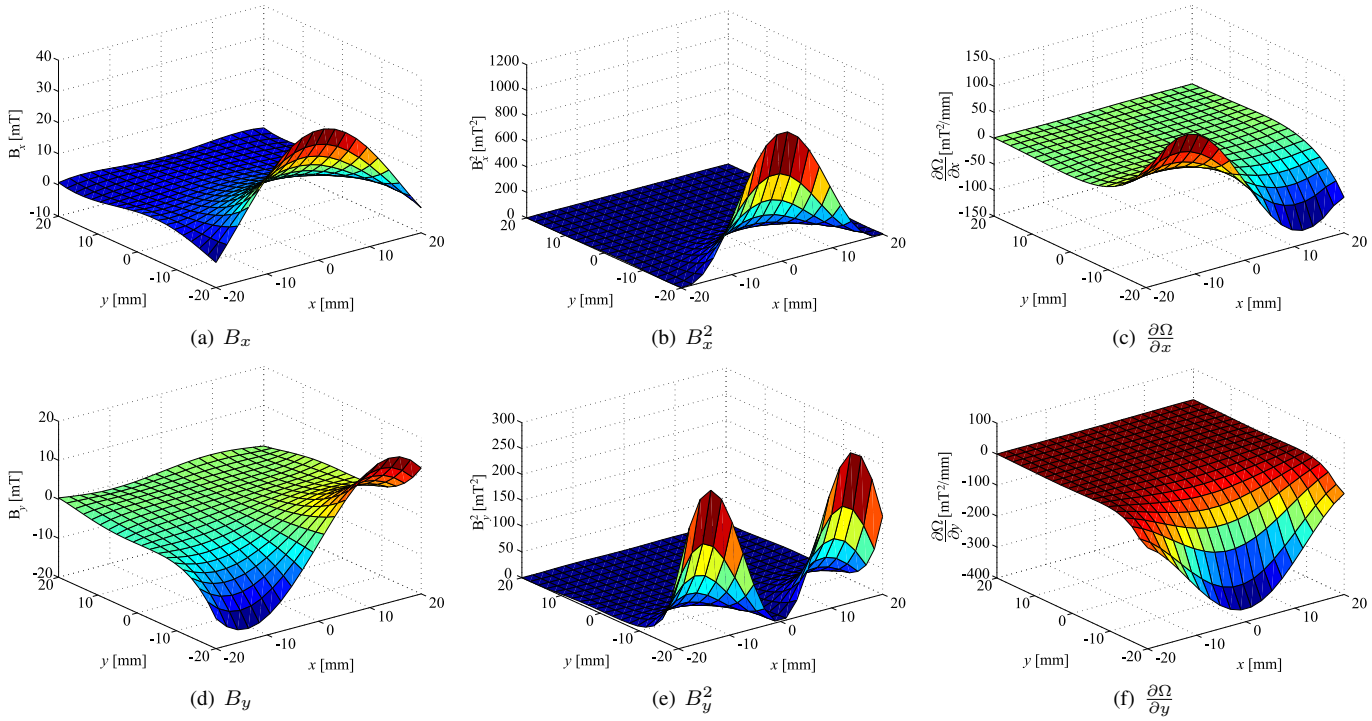

(a) B_x (b) B_x^2 (c) $\frac{\partial \Omega}{\partial x}$

(d) B_y (e) B_y^2 (f) $\frac{\partial \Omega}{\partial y}$

Fig. 2. Results of the finite element (FE) analysis for the gradients of the field-squared in our magnetic system. This system consists of four orthogonally-oriented air-core electromagnets. The FE analysis describes the magnetic field, the field-squared and the gradient of the field-squared within an area of 40×40 mm^2 when a representative current vector of $[0\ 0\ 0\ 1]^{\mathrm{T}}$ A is applied. The entries of the representative current vector are applied to electromagnets A, B, C and D, respectively. The FE results are utilized in the realization of the force-current map (10) and its inverse (13). The gradients of the magnetic field-squared are almost constant within the center of the workspace of our magnetic system (2.4×1.8 mm^2). This observation simplifies the realization of the disturbance force observer and the overall control system since the gradients of the field-squared do not have to be calculated at each point of the workspace. B_x, B_y and Ω are the components of the magnetic field along x-axis, y-axis and the sum of the square of these components, respectively. The FE model is created using Comsol Multiphysics® (COMSOL, Inc., Burlington, U.S.A).

system, shown in Fig. 1. The FE model is verified experimentally, and the deviation between the calculated data of the FE model and the measured values are provided in Table. I. The deviation in the magnitude and angle are calculated for 12 representative points (Fig. 3) that span the workspace of our magnetic system [7], [8]. We consider this deviation as a model mismatch which has to be estimated and compensated by the control system.

The two-dimensional components of the magnetic field can be written, with respect to a basis of orthogonal vectors ($\widehat{\mathbf{x}}$ and $\widehat{\mathbf{y}}$), as

$$\mathbf{B}(\mathbf{P}) = B_x \widehat{\mathbf{x}} + B_y \widehat{\mathbf{y}}. \tag{7}$$

The gradient of the magnetic field-squared $\left(\mathbf{B}^{\mathrm{T}}(\mathbf{P})\mathbf{B}(\mathbf{P})\right)$ can be calculated as follows:

$$\begin{aligned} \nabla\left(\mathbf{B}^{\mathrm{T}}(\mathbf{P})\mathbf{B}(\mathbf{P})\right) &= \nabla\left(B_x^2 + B_y^2\right) = \nabla(\Omega) && (8)\\ &= \frac{\partial \Omega}{\partial x}\widehat{\mathbf{x}} + \frac{\partial \Omega}{\partial y}\widehat{\mathbf{y}}, && (9) \end{aligned}$$

where $\Omega = B_x^2 + B_y^2$ is a scalar function. Substituting (6) in (4) yields

$$\mathbf{F}(\mathbf{P}) = \beta \nabla\left(\mathbf{I}^{\mathrm{T}}\widetilde{\mathbf{B}}^{\mathrm{T}}(\mathbf{P})\widetilde{\mathbf{B}}(\mathbf{P})\mathbf{I}\right), \tag{10}$$

where β is a constant and is given by

$$\beta \triangleq \frac{4}{3}\frac{1}{\mu}\pi r_{\mathrm{p}}^3 \chi_{\mathrm{m}}. \tag{11}$$

Therefore, the components of the magnetic force along x- and y-axis are given by

$$F_j(\mathbf{P}) = \beta \mathbf{I}^{\mathrm{T}} \underbrace{\left(\frac{\partial(\widetilde{\mathbf{B}}^{\mathrm{T}}(\mathbf{P})\widetilde{\mathbf{B}}(\mathbf{P}))}{\partial j}\right)}_{\triangleq \mathbf{\Psi}_j} \mathbf{I} \quad \text{for} \quad j = x, y. \tag{12}$$

where $F_j(\mathbf{P})$ is the magnetic force component for $(j = x, y)$. The forward force-current map (12) provides the magnetic force experienced by the microparticle due to a set of applied currents. The proposed control system utilizes this map along with its inverse (given a set of reference forces, we have to solve (12) for $\mathbf{I}$). The gradients along x- and y-axis within the center of the workspace are almost constant, as shown in Figs. 2(c) and (f), respectively. This observation simplifies the force-current map (12). Nevertheless, the inverse of the quadratic matrix equation ((10) or (12)) has to be solved for the current vector ($\mathbf{I}$).

Necessary and sufficient conditions for the existence of a particular solution for quadratic matrix equations are reported by Shurbet *et al.* [25]. These conditions provide a solution for the inverse of our force-current map (12) of the following form:

$$\begin{aligned} \mathbf{X} = \mathbf{\Psi}_j^{\dagger}\left(F_j \mathbf{\Psi}_j\right)^{\frac{1}{2}} + \left(\mathbf{\Pi} - \mathbf{\Psi}_j^{\dagger}\mathbf{\Psi}_j\right)\Big[F_j((F_j\mathbf{\Psi}_j)^{\frac{1}{2}})^{\dagger} \\ + \mathbf{U}\left(\mathbf{\Pi} - (F_j\mathbf{\Psi}_j)^{\frac{1}{2}}((F_j\mathbf{\Psi}_j)^{\frac{1}{2}})^{\dagger}\right)\Big], \end{aligned} \tag{13}$$

TABLE I

EXPERIMENTAL VALIDATION OF THE FINITE ELEMENT (FE) ANALYSIS BY CALCULATING THE MAGNITUDES ($\|\cdot\|$) AND ANGLE ($\angle(\cdot)$) DEVIATIONS BETWEEN THE MAGNETIC FIELDS PROVIDED BY THE FE ANALYSIS ($\mathbf{B}_{\mathrm{F}}$) AND THE MEASURED MAGNETIC FIELDS ($\mathbf{B}_{\mathrm{M}}$). MEASUREMENTS ARE CARRIED OUT AT 12 REPRESENTATIVE POINTS (P_l FOR ($l = 1, \ldots, 12$)) WHICH SPAN THE WORKSPACE OF THE MAGNETIC SYSTEM USING A CALIBRATED THREE-AXIS HALL MAGNETOMETER (SENTRON AG, DIGITAL TESLAMETER 3MS1-A2D3-2-2T, SWITZERLAND). PLANAR COMPONENTS OF THE MAGNETIC FIELD ARE ONLY PROVIDED SINCE THIS WORK ADDRESSES MOTION CONTROL OF MICROPARTICLES IN A TWO-DIMENSIONAL WORKSPACE.

Point	P_1	P_2	P_3	P_4	P_5	P_6	P_7	P_8	P_9	P_{10}	P_{11}	P_{12}
$\mathbf{B}_{\mathrm{F}}$ [mT]	$\begin{bmatrix}55.2\\-33.6\end{bmatrix}$	$\begin{bmatrix}25\\-11.5\end{bmatrix}$	$\begin{bmatrix}12.5\\-4.8\end{bmatrix}$	$\begin{bmatrix}6.5\\-2.1\end{bmatrix}$	$\begin{bmatrix}82.3\\0.1\end{bmatrix}$	$\begin{bmatrix}31.4\\-0.6\end{bmatrix}$	$\begin{bmatrix}14.4\\-0.4\end{bmatrix}$	$\begin{bmatrix}7.5\\0.0\end{bmatrix}$	$\begin{bmatrix}55.2\\33.6\end{bmatrix}$	$\begin{bmatrix}25\\11.5\end{bmatrix}$	$\begin{bmatrix}12.5\\4.8\end{bmatrix}$	$\begin{bmatrix}6.5\\2.1\end{bmatrix}$
$\mathbf{B}_{\mathrm{M}}$ [mT]	$\begin{bmatrix}48.4\\-28.1\end{bmatrix}$	$\begin{bmatrix}22.9\\-9.9\end{bmatrix}$	$\begin{bmatrix}12.0\\-4.1\end{bmatrix}$	$\begin{bmatrix}7.0\\-1.8\end{bmatrix}$	$\begin{bmatrix}73.6\\0.2\end{bmatrix}$	$\begin{bmatrix}29.4\\0.1\end{bmatrix}$	$\begin{bmatrix}14.2\\0.1\end{bmatrix}$	$\begin{bmatrix}7.9\\0.1\end{bmatrix}$	$\begin{bmatrix}56.2\\27.1\end{bmatrix}$	$\begin{bmatrix}24.8\\9.4\end{bmatrix}$	$\begin{bmatrix}12.8\\3.9\end{bmatrix}$	$\begin{bmatrix}7.4\\2.1\end{bmatrix}$
$\frac{\|\mathbf{B}_{\mathrm{F}}\|}{\|\mathbf{B}_{\mathrm{M}}\|}$	1.15	1.10	1.05	0.94	1.11	1.06	1.01	0.94	1.03	1.03	1.00	0.86
$\angle(\mathbf{B}_{\mathrm{F}}, \mathbf{B}_{\mathrm{M}})$	1.24°	1.38°	2.24°	3.64°	0.09°	1.35°	2.08°	0.75°	5.84°	4.13°	4.25°	2.15°

where $\mathbf{\Pi} \in \mathbb{R}^{e\times e}$ is the identity matrix. Further, $\mathbf{U} \in \mathbb{R}^{e\times e}$ is arbitrary matrix. The last column of the matrix ($\mathbf{X} \in \mathbb{R}^{e\times e}$) represents a solution of the inverse force-current map (12). The square root in (13) is calculated by the diagonalization of ($\mathbf{\Psi}_j$) using a matrix $\mathbf{V}_j$, where $\mathbf{V}_j \in \mathbb{R}^{e\times e}$ is a matrix of the eigenvectors of $\mathbf{\Psi}_j$. The square root of ($\mathbf{\Psi}_j$) is then calculated using $\mathbf{V}_j^{-1}\mathbf{D}_j^{\frac{1}{2}}\mathbf{V}_j$, where $\mathbf{D}_j$ is a diagonal matrix of the eigenvalues of $\mathbf{\Psi}_j$. Simulation results of the inverse map are provided in Fig. 4. Given an arbitrary force component (F_j for $j = x, y$), we calculate the corresponding current vector using (13). In order to verify that (13) indeed provides correct results (vector of current values at each of the electromagnets), the given arbitrary force component is compared to the calculated force using the forward force-current map when the calculated currents are provided as inputs to (12). The difference between the input and the calculated forces for 20 arbitrary force components are shown in Fig. 4(a). We observe that the maximum error between the calculated and input magnetic forces is 0.35 nN (index of simulation 18). Moreover, the inverse force-current map is evaluated for a sinusoidal magnetic force with an exponential envelope $\left(F_j = \frac{1}{\beta_{\mathrm{n}}}\left(0.01 + 0.01\sin(2t)\exp(-0.12t)\right)\right)$. The input force is plotted against the calculated force, as shown in Fig. 4(b). The calculated currents at each of the electromagnets ($e = 4$) are shown in Fig. 4(c). The error between the input and calculated force has maximum value of 0.01 nN (force error of 0.01 nN is equivalent to norm-2 of current error of 0.037 A) when a sinusoidal force input is provided. The quadratic matrix equation (12) is solvable if the matrix $(F_j\mathbf{\Psi}_j)^{\frac{1}{2}}$ exists [25]. Therefore, we attribute the maximum error in Fig. 4(a) to this condition. In this simulation, the $e\times e$ matrix $(\widetilde{\mathbf{B}}^{\mathrm{T}}(\mathbf{P})\widetilde{\mathbf{B}}(\mathbf{P}))$ is provided by the FE model.

III. MODEL MISMATCH AND DISTURBANCE COMPENSATION: INNER-LOOP

During the navigation of a microparticle in a fluid, it experiences drag forces and external forces. We model these forces as a disturbance force input ($\mathbf{d}(\mathbf{P})$). The estimation and compensation this disturbance force would allow for the realization of the nominal model of the magnetic system. The

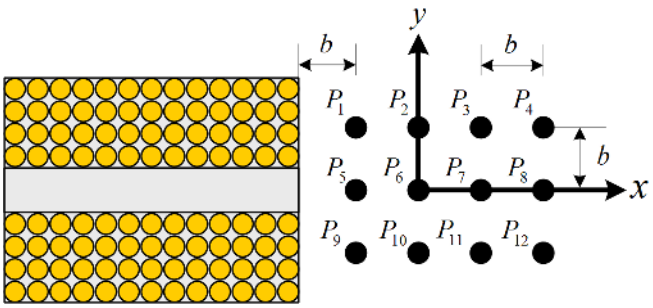

Fig. 3. Measurement of the magnetic field within a grid which spans the workspace of the magnetic system ($b = 10$ mm) to validate the finite element model. The components of the magnetic field are measured at each point of the grid using a calibrated three-axis Hall magnetometer (Sentron AG, Digital Teslameter 3MS1-A2D3-2-2T, Switzerland).

dynamics of the microparticle is given by

$$\mathbf{F}(\mathbf{P}) - \mathbf{d}(\mathbf{P}) = \mathrm{M}\ddot{\mathbf{P}}, \tag{14}$$

where M is the mass of the microparticle. Further, $\mathbf{d}(\mathbf{P}) \in \mathbb{R}^{2\times 1}$ is the planar disturbance force input. This disturbance force can be calculated using the inverse of the nominal model ($G_{\mathrm{n}}(s)$) and the nominal magnetic force input ($\mathbf{F}_{\mathrm{n}}(\mathbf{P})$) as follows:

$$\mathbf{d}_{\mathbf{o}}(\mathbf{P}) = \mathbf{F}_{\mathrm{n}}(\mathbf{P}) - G_{\mathrm{n}}^{-1}(s)\mathbf{P} = \Delta G(s)\mathbf{P} + \mathbf{d}(\mathbf{P}); \tag{15}$$

where $\mathbf{d}_{\mathbf{o}}(\mathbf{P}) \in \mathbb{R}^{2\times 1}$ is the calculated disturbance force based on the nominal model and the nominal magnetic force. Further,

$$G_{\mathrm{n}}(s) = \frac{1}{\mathrm{M}_{\mathrm{n}}s^2} \quad \text{and} \quad \Delta G(s) = G^{-1}(s) - G_{\mathrm{n}}^{-1}(s). \tag{16}$$

In (16), M_{n} is the nominal mass of the microparticle. The nominal magnetic force is given by

$$\mathbf{F}_{\mathrm{n}}(\mathbf{P}) = \beta_{\mathrm{n}}\nabla\left(\mathbf{I}^{\mathrm{T}}\widetilde{\mathbf{B}}_{\mathrm{n}}^{\mathrm{T}}(\mathbf{P})\widetilde{\mathbf{B}}_{\mathrm{n}}(\mathbf{P})\mathbf{I}\right), \tag{17}$$

where the subscript (n) denotes the nominal values of the parameter (β) and the matrix ($\widetilde{\mathbf{B}}^{\mathrm{T}}(\mathbf{P})\widetilde{\mathbf{B}}(\mathbf{P})$), respectively. The calculated disturbance force ($\mathbf{d}_{\mathbf{o}}(\mathbf{P})$) consists not only of the disturbance force ($\mathbf{d}(\mathbf{P})$) but also of the perturbation ($\Delta G(s)$) between the actual system and the nominal model based on (15). The inverse of the nominal model ($G_{\mathrm{n}}^{-1}(s)$) cannot be realized since it includes derivatives. Therefore,

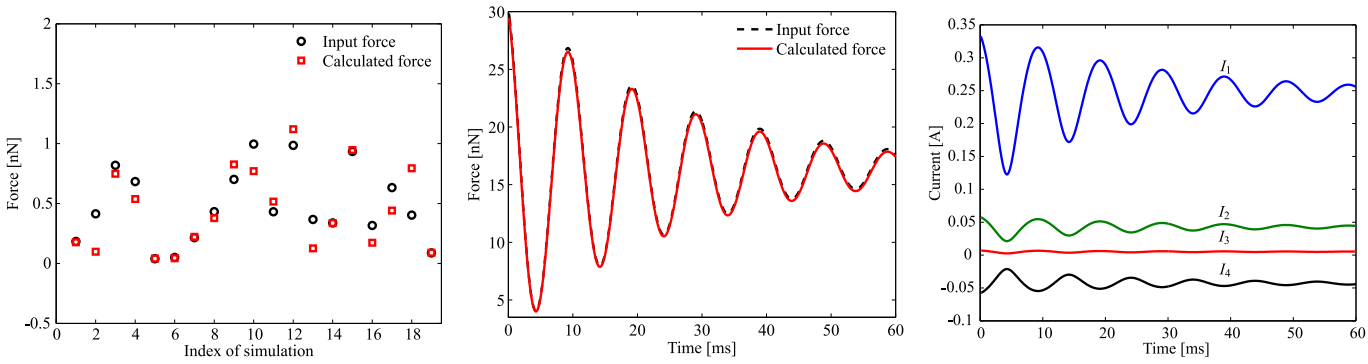

(a) Input versus calculated forces (b) Input versus calculated forces (c) Calculated currents

Fig. 4. Calculation of the current vector using the inverse of the force-current map (12). The quadratic matrix equation is used to determine the current at each of the four electromagnets [25]. (a) The current vector ($\mathbf{I} \in \mathbb{R}^{4\times 1}$) is calculated for 20 arbitrary force components. The input forces are compared to the computed forces using the calculated current vector to verify the result of the inverse force-current map. The black circles represent the values of the arbitrary input forces, whereas the red squares represent the calculated forces from the computed current vectors. (b) Input versus calculated force values. The dashed black lines represent the input values of the force, whereas the red line represents the calculated force using the currents which are determined by the inverse force-current map. The deviation between the input and calculated forces has maximum calculation error of 0.01 nN which corresponds to norm-2 of current error of 0.037 A. The input force has the following representation: $F_j = \frac{1}{\beta_{\rm n}}(0.01 + 0.01\sin(2t)\exp(-0.12t))$ (c) Currents are calculated by the solution (13) of the inverse of the force-current map for the time-varying force with an exponential envelope. I_i for $(i = 1, \ldots, e)$ represents the current at the ith electromagnet of our magnetic system.

the disturbance force must be determined through a low-pass filter $(Q(s))$

$$\widehat{\mathbf{d}}(\mathbf{P}) = Q(s)\mathbf{d}_{\mathbf{o}}(\mathbf{P}) = Q(s)\big(\mathbf{F}_{\rm n}(\mathbf{P}) - G_{\rm n}^{-1}(s)\mathbf{P}\big), \qquad (18)$$

where $\widehat{\mathbf{d}}(\mathbf{P}) \in \mathbb{R}^{2\times 1}$ is the estimated disturbance force through the low-pass filter. Degree of $Q(s)$ depends on the order of the nominal plant $(G_{\rm n}(s))$. Integrating the disturbance force observer (18) with a feedback control system affects its stability and performance. This effect can be shown by analyzing the frequency response of [26]

$$Z(s) = \frac{Q(s)}{1 - Q(s)} G_{\rm n}^{-1}(s), \qquad (19)$$

In (19), $Z(s)$ is a transfer function that determines the characteristics of the observer-based feedback control system. Fig. 5 provides the frequency response of $Z(s)$ for different orders of $Q(s)$. Increasing the order of $Q(s)$ allows for the realization of the nominal model for different types of plants. However, the corresponding stability deteriorates due to the increased phase lag, as shown in the phase diagram of Fig. 5. This tradeoff between stability and performance has to be considered during the design of (18) by selecting the proper order and gains of its associated low-pass filter $(Q(s))$.

The purpose of estimating the disturbance forces (experienced by the microparticle) is to achieve robustness of the motion control system by rejecting these disturbances using an inner-loop (Fig. 6). This robustness can be achieved by converting the estimated disturbance force into compensating control input at each of the electromagnets of the magnetic system. The force-current map (12) is derived in Section II. Therefore, the compensating current input can be determined by solving (10) when $\mathbf{F}(\mathbf{P})$ is set to $\widehat{\mathbf{d}}(\mathbf{P})$.

Implementation of the observer (18) requires measuring one of the outputs of the magnetic system based on the available measurement (position of the microparticle). In addition, the input current or force has to be known and used in the realization of (18). In the previous analysis, the measurement noise is ignored. However, in practice it has a significant influence on the performance of the observer-based feedback system. Therefore, we rewrite (18) by accounting for the measurement noise (ξ)

$$\widehat{\mathbf{d}}(\mathbf{P}) = Q(s)\left(\mathbf{F}_{\rm n}(\mathbf{P}) - G_{\rm n}^{-1}(s)(\mathbf{P} - \xi)\right). \qquad (20)$$

Feeding the estimated disturbance force into a feedback control system would result in the following output position [26]:

$$\mathbf{P} = \frac{G_{\rm n}(s)\left(\mathbf{I}_{\rm ref} - (1 - Q(s))\mathbf{d}(\mathbf{P})\right) + Q(s)\xi}{1 + (1 - Q(s))\,\Delta G(s) G_{\rm n}(s)}, \qquad (21)$$

where $\mathbf{I}_{\rm ref}$ is the control input of an outer-loop which will be determined. Equation (21) shows that, $Q(s)$ represents a sensitivity function to the sensor noise, whereas $(1 - Q(s))$ represents a sensitivity function to the mismatch between the system and the nominal model. Therefore, due to the presence of inevitable measurement noise (ξ), the bandwidth of the observer (20) is limited by the bandwidth of the measurement noise. The tradeoff (between stability and performance) and constraint (limits on the bandwidth) analyzed by (19) and (21), respectively, must be considered during the design of the disturbance force observer. This can be accomplished by selecting a proper order of $Q(s)$ and calculating its associated gains. We observe that a first-order low-pass filter with a cut-off frequency of 30 rad/s, satisfies the tradeoff between stability and performance. We benefit from the low frequency range at which manipulation of microparticles generally occurs by filtering the high frequency noise without affecting the performance. Since the effect of the measurement noise is determined by (21), we ignore its effect in the following analysis for simplicity. Rewriting (18) using a first-order low-pass filter for $Q(s)$ [20]

$$\dot{\widehat{\mathbf{d}}}(\mathbf{P}) = -g\widehat{\mathbf{d}}(\mathbf{P}) + g\left(\mathbf{F}_{\rm n}(\mathbf{P}) - \mathrm{M}_{\rm n}\ddot{\mathbf{P}}\right), \qquad (22)$$

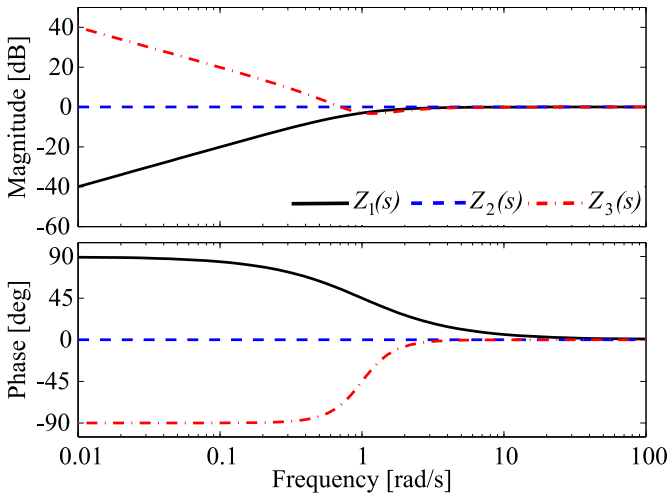

Fig. 5. Characteristics of the observer-based feedback control system for different orders of $Q(s)$. The order of the observer affects the stability of the observer-based feedback control system. The frequency response of $Z(s)$ is plotted for different degrees of $Q(s)$. The index of the transfer function $Z_k(s)$ stands for the order of $Q(s)$ ($k = 1$ indicates that $Q(s)$ is a first-order transfer function).

where $\mathrm{M_n}$ and g are the nominal mass of the microparticle and the cut-off frequency of the first-order low-pass filter. Nominal parameters and variables (denoted with the subscript n) are used in the realization of the disturbance force observer. The disturbance force estimation error ($\mathbf{e_d} = \mathbf{d}(\mathbf{P}) - \widehat{\mathbf{d}}(\mathbf{P})$) can be determined using (14) and (18). Therefore, the estimation error dynamics is given by

$$\dot{\mathbf{e}}_\mathbf{d} = \dot{\mathbf{d}}(\mathbf{P}) - \dot{\widehat{\mathbf{d}}}(\mathbf{P}). \tag{23}$$

We further assume that the disturbance force varies slowly ($\dot{\mathbf{d}}(\mathbf{P}) = 0$). Therefore, the estimation error is

$$\dot{\mathbf{e}}_\mathbf{d} + g\mathbf{e}_\mathbf{d} = 0. \tag{24}$$

This error dynamics indicates that the estimated disturbance force will converge to the actual one in finite time. Nevertheless, we define auxiliary functions to avoid the realization of the estimated disturbance force through the acceleration of the microparticle [14]

$$\mathbf{\Gamma} = \widehat{\mathbf{d}}(\mathbf{P}) - \Phi(\dot{\mathbf{P}}), \tag{25}$$

where $\mathbf{\Gamma}$ and $\Phi(\dot{\mathbf{P}})$ are auxiliary functions. In (25), $\mathbf{\Gamma}$ provides a change of variables to avoid measuring the acceleration of the microparticle, whereas $\Phi(\dot{\mathbf{P}})$ is a function of the velocity of the microparticle (to be determined). The time derivative of (25) yields

$$\dot{\mathbf{\Gamma}} = \dot{\widehat{\mathbf{d}}}(\mathbf{P}) - \frac{\partial \Phi(\dot{\mathbf{P}})}{\partial \dot{\mathbf{P}}}\ddot{\mathbf{P}}. \tag{26}$$

Substituting (25) and (26) in (22)

$$\dot{\mathbf{\Gamma}} + \frac{\partial \Phi(\dot{\mathbf{P}})}{\partial \dot{\mathbf{P}}}\ddot{\mathbf{P}} = g\left(\mathbf{F}_\mathrm{n}(\mathbf{P}) - \mathrm{M_n}\ddot{\mathbf{P}}\right) - g\left(\mathbf{\Gamma} + \Phi(\dot{\mathbf{P}})\right). \tag{27}$$

Setting the derivative of the auxiliary function, $\frac{\partial \Phi(\dot{\mathbf{P}})}{\partial \dot{\mathbf{P}}} = -g\mathrm{M_n}$, yields the following representation of the disturbance force observer using ($\mathbf{\Gamma}$):

$$\dot{\mathbf{\Gamma}} = -g\left(\mathbf{\Gamma} + \Phi(\dot{\mathbf{P}})\right) + g\mathbf{F}_\mathrm{n}(\mathbf{P}). \tag{28}$$

where the auxiliary function $\Phi(\dot{\mathbf{P}})$ is

$$\Phi(\dot{\mathbf{P}}) = -g\mathrm{M_n}\dot{\mathbf{P}}. \tag{29}$$

Taking the Laplace transform of (28) without changing the notations of the variables

$$\mathbf{\Gamma} = \frac{g}{s+g}\left(\mathbf{F}_\mathrm{n}(\mathbf{P}) - \Phi(\dot{\mathbf{P}})\right). \tag{30}$$

Finally, substituting (30) in (25) yields

$$\widehat{\mathbf{d}}(\mathbf{P}) = \frac{g}{s+g}\left(\mathbf{F}_\mathrm{n}(\mathbf{P}) - \Phi(\dot{\mathbf{P}})\right) + \Phi(\dot{\mathbf{P}}). \tag{31}$$

Estimating the disturbance force ($\widehat{\mathbf{d}}(\mathbf{P})$) requires measuring the velocity of the microparticle and the input current vector. In (31), the nominal magnetic force ($\mathbf{F}_\mathrm{n}(\mathbf{P})$) can be represented explicitly in terms of the input current ($\mathbf{I}$) using the nominal forward force-current map (17). The disturbance force observer is shown in Fig. 6. The force-current map is used to convert the estimated disturbance force into equivalent currents to simultaneously attenuate the disturbance forces. As shown in Fig. 6, the disturbance force observer depends on the nominal values of the parameters of the magnetic system. The deviation between these parameters and their actual values is modeled as a disturbance force in the magnetic system. The disturbance force observer just represents an inner-loop for the control system. Stability of the overall control system must be achieved by an outer-loop.

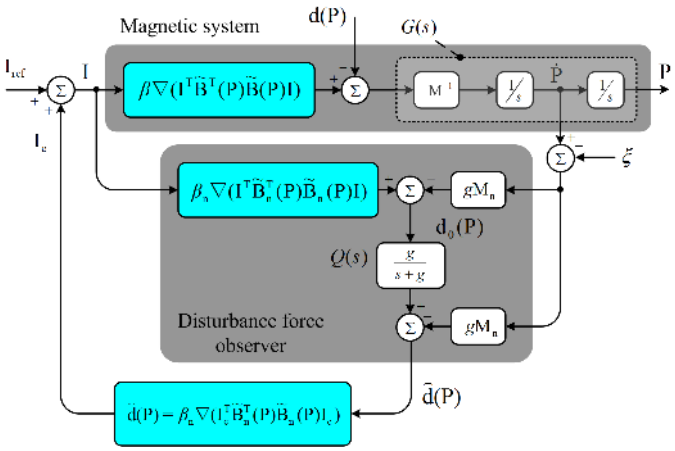

Fig. 6. Disturbance force estimation and compensation. The force-current map along with its inverse are utilized to determine the estimated disturbance force and provide a compensating current input ($\mathbf{I}_\mathrm{c}$) to reject the disturbance force input ($\mathbf{d}(\mathbf{P})$). The observer is based on the nominal values of the parameters of the magnetic system denoted with the subscript n. The matrix ($\widetilde{\mathbf{B}}_\mathrm{n}^\mathrm{T}(\mathbf{P})\widetilde{\mathbf{B}}_\mathrm{n}(\mathbf{P})$) does not have to be evaluated at each point of the workspace since it has almost a constant value based on the finite element analysis of our magnetic system. $\mathbf{d}(\mathbf{P})$, $\mathbf{d_o}(\mathbf{P})$ and $\widehat{\mathbf{d}}(\mathbf{P})$ represent the input disturbance force, calculated disturbance force using the nominal model of the system and the estimated disturbance force through the low-pass filter ($Q(s)$), respectively. The turquoise blocks indicate that the input is evaluated based on (17).

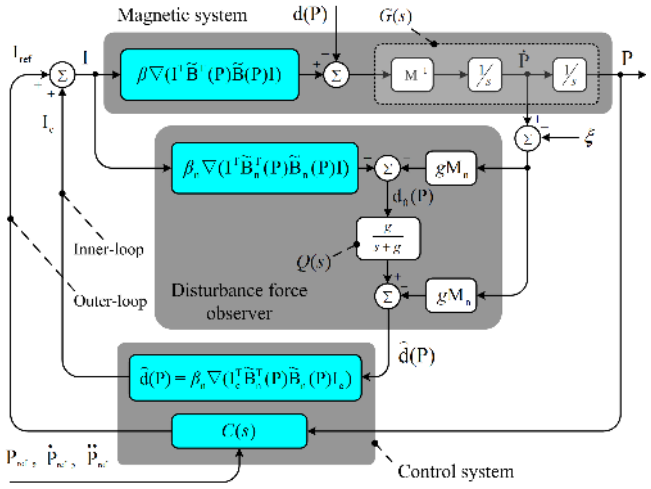

Fig. 7. Overall structure of the control system: The control system consists of inner- and outer-loops to compensate for the disturbances and achieve stability, respectively. The outer-loop control transfer function ($C(s)$) is determined using (35). The disturbance force observer is based on the nominal values of the parameters of the magnetic system denoted with the subscript n. The matrix ($\widetilde{\mathbf{B}}_{\mathrm{n}}^{\mathrm{T}}(\mathbf{P})\widetilde{\mathbf{B}}_{\mathrm{n}}(\mathbf{P})$) does not have to be evaluated at each point of the workspace since it has almost a constant value based on the finite element analysis of our magnetic system. $\mathbf{d}(\mathbf{P})$, $\mathbf{d_o}(\mathbf{P})$ and $\widehat{\mathbf{d}}(\mathbf{P})$ are the input disturbance force, calculated disturbance force using the nominal model of the magnetic system and the estimated disturbance force through the low-pass filter ($Q(s)$), respectively. The turquoise blocks indicate that the input is evaluated based on (17) and (35).

IV. Motion Control Design: Outer-Loop

Dynamics of our magnetic system has to be stabilized by an outer-loop control input. The outer-loop is necessary since a stable equilibrium point under static magnetic forces cannot be achieved [27]. This claim can be verified by calculating the divergence of the magnetic force given by (4) at a point within the workspace of our magnetic system. By considering a point ($\mathbf{P}$) under static force, i.e., $\mathbf{F}(\mathbf{P}) = 0$, the necessary condition for this point to be a stable equilibrium point is

$$\nabla \cdot \left(\frac{4}{3} \frac{1}{\mu} \pi r_{\mathrm{p}}^{3} \chi_{\mathrm{m}} \nabla \left(\mathbf{B}^{\mathrm{T}}(\mathbf{P}) \mathbf{B}(\mathbf{P}) \right) \right) < 0. \tag{32}$$

Since all the arguments of (32) are positive (with the exception of χ_{m} for diamagnetic materials, which are not considered in our work) [24], stable equilibrium point cannot be achieved without feedback control inputs. Therefore, we devise a control law of the following form:

$$\mathbf{I} = \mathbf{I}_{\mathrm{c}} + \mathbf{I}_{\mathrm{ref}}, \tag{33}$$

where $\mathbf{I}_{\mathrm{c}}$ and $\mathbf{I}_{\mathrm{ref}}$ are the control inputs of the inner- and outer-loops, respectively. Using the estimated disturbance force ($\widehat{\mathbf{d}}(\mathbf{P})$) by (31), we can calculate $\mathbf{I}_{\mathrm{c}}$ using

$$\widehat{\mathbf{d}}(\mathbf{P}) - \beta_{\mathrm{n}} \nabla \left(\mathbf{I}_{\mathrm{c}}^{\mathrm{T}} \widetilde{\mathbf{B}}_{\mathrm{n}}^{\mathrm{T}}(\mathbf{P}) \widetilde{\mathbf{B}}_{\mathrm{n}}(\mathbf{P}) \mathbf{I}_{\mathrm{c}} \right) = 0. \tag{34}$$

The estimated disturbance force-current map (34) is solved using (13) and the two-dimensional components of the estimated disturbance force.

The control input of the outer-loop has to achieve stability for the overall magnetic system. Therefore, we devise an outer-loop of the following form:

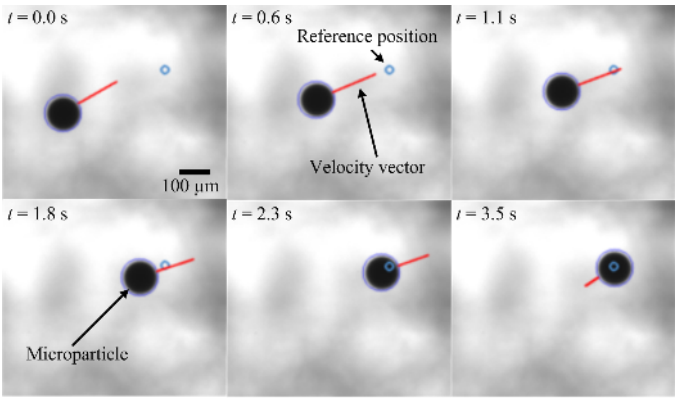

Fig. 8. Microparticle moving towards a reference position under the influence of the controlled fields generated by the control law (33). The microparticle tracks the given reference position at velocity of 98 μm/s and settling time of 3.15 s. In the steady-state, the position tracking error is 10 μm. The large blue circle indicates the tracked microparticle by our feature tracking software [12], whereas the small blue circle indicates the reference position. The velocity vector of the microparticle is represented by the red line. The controller gains are: $k_{\mathrm{p1}} = k_{\mathrm{p2}} = 0.1\ \mathrm{s}^{-2}$ and $k_{\mathrm{d1}} = k_{\mathrm{d2}} = 0.5\ \mathrm{s}^{-1}$. The cut-off frequency of the low-pass filter associated with the disturbance force observer is 30 rad/s.

$$\mathbf{F}_{\mathrm{ref}}(\mathbf{P}) = \mathrm{M_n} \left(\ddot{\mathbf{P}}_{\mathrm{ref}} - \mathbf{K_d}\dot{\mathbf{e}} - \mathbf{K_p}\mathbf{e} \right), \tag{35}$$

where $\mathbf{F}_{\mathrm{ref}}(\mathbf{P})$ and $\ddot{\mathbf{P}}_{\mathrm{ref}}$ are the outer-loop force and the reference acceleration input, respectively. Further, $\dot{\mathbf{e}} = \dot{\mathbf{P}}_{\mathrm{ref}} - \dot{\mathbf{P}}$, is the velocity tracking error of the microparticle and similarly, $\mathbf{e} = \mathbf{P}_{\mathrm{ref}} - \mathbf{P}$, is the position tracking error. The reference position vector ($\mathbf{P}_{\mathrm{ref}}$) and velocity vector ($\dot{\mathbf{P}}_{\mathrm{ref}}$) are known beforehand. The controller gain matrices ($\mathbf{K_p} > 0$ and $\mathbf{K_d} > 0$) must achieve stable tracking error dynamics. The gain matrices of (35) are

$$\mathbf{K_p} = \begin{bmatrix} k_{\mathrm{p1}} & 0 \\ 0 & k_{\mathrm{p2}} \end{bmatrix} \text{ and } \mathbf{K_d} = \begin{bmatrix} k_{\mathrm{d1}} & 0 \\ 0 & k_{\mathrm{d2}} \end{bmatrix}, \tag{36}$$

where $k_{\mathrm{p}i}$ and $k_{\mathrm{d}i}$, for $(i = 1, 2)$, are the proportional and derivative gains, respectively. The outer-loop control input ($\mathbf{I}_{\mathrm{ref}}$) can be calculated by

$$\mathbf{F}_{\mathrm{ref}}(\mathbf{P}) - \beta_{\mathrm{n}} \nabla \left(\mathbf{I}_{\mathrm{ref}}^{\mathrm{T}} \widetilde{\mathbf{B}}_{\mathrm{n}}^{\mathrm{T}}(\mathbf{P}) \widetilde{\mathbf{B}}_{\mathrm{n}}(\mathbf{P}) \mathbf{I}_{\mathrm{ref}} \right) = 0. \tag{37}$$

The control input (33) results in the following magnetic force:

$$\mathbf{F}(\mathbf{P}) = \widehat{\mathbf{d}}(\mathbf{P}) + \mathbf{F}_{\mathrm{ref}}(\mathbf{P}). \tag{38}$$

Substituting (31), (35) and (38) into (14), we obtain

$$\ddot{\mathbf{e}} + \mathbf{K_d}\dot{\mathbf{e}} + \mathbf{K_p}\mathbf{e} = 0. \tag{39}$$

Compensating for the model mismatch and disturbances along with selecting positive definite control gain matrices ($\mathbf{K_p} > 0$ and $\mathbf{K_d} > 0$), enforces the position tracking error to zero in finite time based on (39). We assume that the estimated disturbance force converges to the actual one based on (24). The overall structure of the control system is provided by Fig. 7.

TABLE II
EXPERIMENTAL PARAMETERS AND CONTROLLER GAINS. THE CONTROLLER GAINS ARE SELECTED SUCH THAT THE MATRICES $(\mathbf{K_P})$ AND $(\mathbf{K_d})$ ARE POSITIVE DEFINITE.

Parameter	Value	Parameter	Value
$\max I_i$ [A]	1.0	$\max \lvert\mathbf{B}(\mathbf{P})\rvert$ [mT]	15
η [mPa.s]	1.0	$\max \lvert\nabla(\mathbf{B}^{\mathrm{T}}\mathbf{B})\rvert$ [mT^2/m]	5
r_{p} [μm]	50	μ_0 [T.m/A]	$4\pi \times 10^{-7}$
$k_{\mathrm{p1,2}}$ [s^{-2}]	0.1	χ_{m}	0.075
$k_{\mathrm{d1,2}}$ [s^{-1}]	0.5	$\mathrm{M_n}$ [kg]	7.33×10^{-10}
g [rad/s]	30	Workspace [mm^2]	2.4×1.8

TABLE III
CHARACTERISTICS OF THE CONTROL SYSTEM IN THE TRANSIENT- AND STEADY-STATES. THE TRANSIENT-STATE IS REPRESENTED BY THE AVERAGE SETTLING TIME AND AVERAGE VELOCITY, WHEREAS THE STEADY STATE IS REPRESENTED BY THE MAXIMUM ERROR. THE AVERAGE IS CALCULATED FROM 10 CLOSED-LOOP CONTROL TRIALS WHEN DISTURBANCE FORCES ARE UNCOMPENSATED AND COMPENSATED.

Criterion	Uncompensated	Compensated
Average settling time [s]	3.6 ± 0.4	3.0 ± 0.3
Average speed [μm/s]	45 ± 5.8	60 ± 7.8
Maximum error [μm]	18	14

V. EXPERIMENTAL RESULTS

The experiments are done using a magnetic system with four orthogonally-oriented air-core electromagnets [12]-[13]. The electromagnets surround a water reservoir, as shown in Fig. 1. The microparticles utilized throughout our experiments are super-paramagnetic particles made by embedding magnetite (Fe_3O_4) in a matrix of poly(D,L-lactic acid). According to the manufacturer (PLAParticles-M-redF-plain from Micromod Partikeltechnologie GmbH, Rostock-Warnemuende, Germany), their average diameter is 100 μm , magnetization at 100 mT is approximately 4.3 Am^2/kg and they do not saturate until 1 T. Since the density of the particles is 1.4×10^3 kg/m^3, we estimate the susceptibility χ_{m} to be 0.075 (Table II). The position of the microparticle is tracked using a vision system embedded to a microscope.

In order to implement our control system, the inner- and outer-loops are realized. The inner-loop depends on the disturbance force observer (31), whereas the outer-loop stabilizes the dynamics of the magnetic system using (35). These loops depend on the position and velocity of the microparticle. The disturbance force observer depends on the availability of the outputs of the magnetic system (position or velocity of the microparticle) along with assuming that the nominal model of the magnetic force is known *a priori*. We calculate the velocity of the microparticle along with the input currents to realize the disturbance force observer (31). Presence of measurement noise could deteriorate the performance of the disturbance force observer and limit its bandwidth, as explained in Section III. Therefore, velocity of the microparticle is calculated using a low-pass filter with a cut-off frequency of 30 rad/s.

The disturbance force observer estimates the components of the disturbance force along x- and y-axis. Velocities along these axes are fed into the observer along with the magnetic force input calculated based on the nominal model (17). Hereafter, the compensating currents $(\mathbf{I}_{\mathrm{c}})$ is determined by solving (34). The transfer function of the outer-loop control system $(C(s))$ is determined using the control law (35).

The experimental result of the motion control law (33) is provided in Fig. 8. This control law allows for the tracking of a reference position within the workspace of the system while simultaneously compensating for the disturbance force experienced by the microparticle. As shown in Fig. 8, the controlled microparticle tracks a 300 μm reference position (distance between the initial position of the microparticle and the given reference position) at a velocity of 98 μm/s and settling time of 3.15 s. In the steady-state, the position tracking error is 10 μm. In order to show that the proposed control system indeed compensates for the disturbance force, we investigate its performance in the presence and absence of the contribution of the inner-loop (this loop estimates the disturbance force and provides a compensating control input). Characteristics of the transient- and steady-states are used to evaluate the performance of the control system in each case.

The experimental validation of the disturbance force compensation by the inner-loop is provided in Figs. 9. Multiple reference positions are given within the workspace of our magnetic system. Figs. 9(a), (b) and (c) provide a representative motion control trial when the output of the inner-loop is not supplied to the magnetic system, whereas Figs. 9(a), (b) and (c) provide a representative motion control trial of the overall control law (33). The position tracking along x- and y-axis provided in Figs. 9(a) and (b), respectively, indicate that the control system achieves average settling time of 3.6 s in the absence of the contribution of the inner-loop. On the other hand, Figs. 9(d) and (e) indicate that the average settling time is 3.0 s when the contribution of the inner-loop is added to the overall control input. In addition, the average velocity of the microparticle is 45 μm/s in the absence of the contribution of the inner-loop, whereas the average velocity is 60 μm/s when the disturbance force is compensated using (31). The average is calculated from 10 motion control trails for each case. The position tracking errors along x- and y-axis for the aforementioned two cases are provided in Fig. 9(c) and Fig. 9(f), respectively. These results show the effect of the inner-loop on the characteristics of the steady-state. The control system achieves maximum position tracking error of 18 μm in the absence of the contribution of the inner-loop, whereas the overall control system (33) achieves maximum position tracking error of 14 μm in the steady-state. Table III summarizes the experimental results. We observe that the microparticle exhibits oscillatory response in the steady-state as shown in Figs. 9(a) and (b) and Figs. 9(d) and (e). This response can be explained by (32), which indicates that a stable equilibrium point cannot be achieved for microparticles of paramagnetic material without a feedback control system.

VI. DISCUSSION

During the design of controllers for magnetic-based manipulation systems, a magnetic force-current map (and magnetic torque-current map) has to be realized and used as a basis of the control system design. This magnetic force-current map

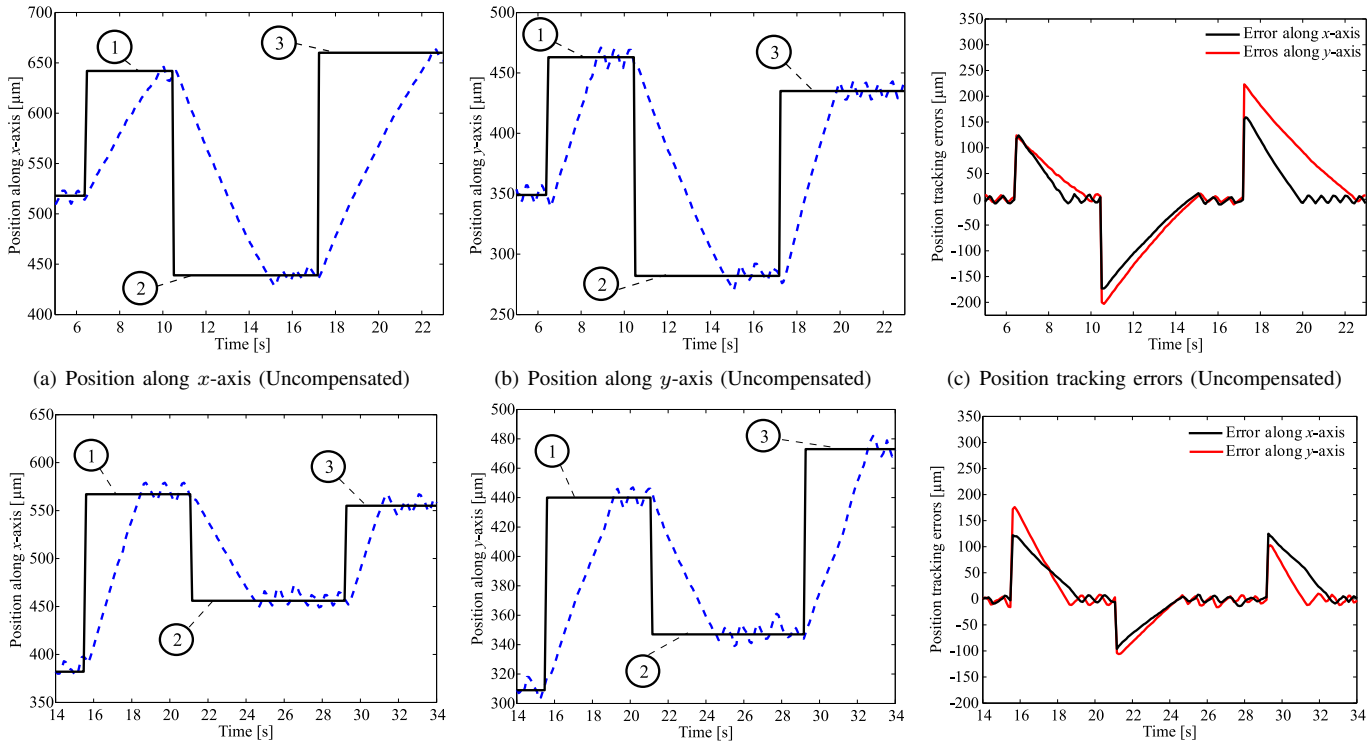

(a) Position along x-axis (Uncompensated) (b) Position along y-axis (Uncompensated) (c) Position tracking errors (Uncompensated)

(d) Position along x-axis (Compensated) (e) Position along y-axis (Compensated) (f) Position tracking errors (Compensated)

Fig. 9. Representative motion control experimental results of the microparticle under the influence of the applied magnetic fields in the absence and presence of the contribution of the inner-loop (with disturbance compensation). The microparticle tracks four different points within the planar workspace of the magnetic system. The reference positions are indicated with ①, ② and ③. The black lines represent the reference set points along x-axis and y-axis, whereas the blue dashed lines represent the path taken by the microparticle. (a and d) Controlled motion of the microparticle along x-axis. (b and e) Controlled motion of the microparticle along y-axis. (c and f) Position tracking errors along x- and y-axis. This motion control result is accomplished by the control law (33).

depends on a field-current map. We model this field-current map by a FE model, and calculate the deviations between its fields and the actual fields measured by a calibrated Hall magnetometer. The average deviation in the magnitude and direction of the magnetic field are 2.3% and 0.7%, respectively. This average is calculated from a grid of 12 points which span the workspace of our magnetic system (Table I). The mismatch between the actual magnetic system and our FE model, along with the drag forces and any unmodeled dynamics are considered as an input disturbance force on the nominal magnetic force-current map. Using this map, a disturbance force observer is designed. This observer allows the estimated disturbance to converge to the actual disturbance force in finite time based on (24). The disturbance force observer is further utilized in the realization of the control system. The control system employs the disturbance force observer in an inner-loop to compensate simultaneously for the disturbance force input (which represents the sum of the aforementioned forces). In addition, overall stability of the magnetic system is achieved by an outer-loop. Realization of the proposed control system relies on the nominal force-current map along with its inverse map (we have shown through simulation results the solution of the inverse map). Furthermore, our FE analysis shows that the gradients of the field-squared do not have to be evaluated at each point of the workspace of our magnetic system since they are almost uniform. This observation along with the solution of the inverse force-current map allows for the realization of the proposed control system.

The order of the low-pass filter $(Q(s))$ associated with the disturbance force observer depends on the nature of the input disturbance force. This force is a function of time and can be modeled by the following polynomial [26]:

$$\frac{d^l}{dt^l}\mathbf{d}(\mathbf{P},t)=0, \tag{40}$$

where $\mathbf{d}(\mathbf{P},t)$ is the input disturbance force and l is the order of the low-pass filter $(Q(s))$ associated with the disturbance force observer. Approximating the input disturbance force using a step function $(l=1)$ allows us to use a first-order low-pass filter in (31). Further, approximating the input disturbance force using a ramp function $(l=2)$ allows us to use a second-order low-pass filter, and so forth. Therefore, our disturbance force observer can be adapted to estimate disturbance force inputs of higher orders.

Even though the experimental work is done using paramagnetic microparticles of spherical geometry, the presented control system is fairly general and can be modified to control super-paramagnetic particles, ferromagnetic particles, microparticles of irregular shapes, and microrobots. This necessitates the incorporation of the magnetic torque-current map with the control system. The magnetic force- and torque-current maps can be used in the realization of the inner- and outer-loops of the control system. Further, the proposed magnetic-based control strategy can be adapted to control microparticles in the three-dimensional space.

A. Conclusions

The mismatch between the actual and nominal field-current map of magnetic-based manipulation systems, which can be as high as 20%, affects the governing force-current map which is necessary for the realization of the magnetic-based control system. In this study, a control system is investigated based on estimating the mismatch and the drag forces. These forces are considered as a disturbance force input to the governing equation of the magnetic system. The outlined control system compensates for this force by an inner-loop. This loop estimates the disturbance force and converts it into a control input for the realization of the nominal model of the magnetic system. In addition, the control system achieves stable position tracking error dynamics for the microparticles using an outer-loop. Compensating the mismatch and the drag forces results in 17% faster response and 23% higher positioning accuracy of the microparticle by the proposed control system in the transient- and steady-states, as opposed to the same control system without compensation.

B. Future Work

Future work in the field of wireless magnetic-based control will be extended to achieve targeted drug delivery. Our microparticles will be coated with drugs and the physiological conditions of the release process will be studied experimentally. Clusters of nanopaticles will be used as magnetic drug carriers owing to their low toxicity and excellent magnetic saturation [28]. Further, we will investigate the possibilities to modify our system to be integrated with a clinical imaging modality, such as magnetic resonance imaging [29]. *In vivo* experiments need to be done to investigate important aspects such as time-varying fluid viscosity and flow. Further, our magnetic system will be modified to incorporate controlled disturbance inputs, such as time-varying fluid flow, to verify the effectiveness of the control technique.

REFERENCES

[1] R. Sinha, G. J. Kim, S. Nie, and D. M. Shin, "Nanotechnology in cancer therapeutics: bioconjugated nanoparticles for drug delivery," *Molecular Cancer Therapeutics*, Vol. 5, no. 8, pp. 1909-1917, August 2006.

[2] B. J. Nelson, I. K. Kaliakatsos, and J. J. Abbott, "Microrobots for minimally invasive medicine," *Annual Review of Biomedical Engineering*, vol. 12, pp. 55-85, April 2010.

[3] V. I. Furdui, J. K. Kariuki, and D. J. Harrison, "Microfabricated electrolysis pump system for isolating rare cells in blood," *Journal of Micromechanics and Microengineering*, vol. 13, no. 4, pp. 164-170, May 2003.

[4] Q. A. Pankhurst, J. Connolly, S. K. Jones, and J. Dobson, "Applications of magnetic nanoparticles in biomedicine," *Journal of Physics*, Vol. 36, no. 13, pp.167-181, July 2003.

[5] A. S. Lubbe, C. Bergemann, J. Brock, and D. G. McClure, "Physiological aspects in magnetic drug-targeting," *Journal of Magnetism and Magnetic Materials*, Vol. 194, no. 1-3, pp. 149-155, April 1999.

[6] J. J. Abbott, Z. Nagy, F. Beyeler, and B. J. Nelson, "Robotics in the small, part I: microbotics," *IEEE Robotics and Automation Magazine*, vol. 14, no. 2, pp. 92-103, June 2007.

[7] M. P. Kummer, J. J. Abbott, B. E. Kartochvil, R. Borer, A. Sengul, and B. J. Nelson, "OctoMag: an electromagnetic system for 5-DOF wireless micromanipulation," *IEEE Transactions on Robotics*, vol. 26, no. 6, pp. 1006-1017, December 2010.

[8] B. E. Kratochvil, M. P. Kummer, S. Erni, R. Borer, D. R. Frutiger, S. Schurle, and B. J. Nelson, "MiniMag: a hemispherical electromagnetic system for 5-DOF wireless micromanipulation," *Proceeding of the 12th International Symposium on Experimental Robotics*, New Delhi, India, December 2010.

[9] J. J. Abbott, O. Ergeneman, M. P. Kummer, A. M. Hirt, and B. J. Nelson, "Modeling magnetic torque and force for controlled manipulation of soft-magnetic bodies," *IEEE Transactions on Robotics and Automation*, vol. 23, no. 6, pp. 1247-1252, December 2007.

[10] S. S. Shevkoplyas, A. C. Siegel, R. M. Westervelt, M. G. Prentiss, and G. M. Whitesides, "The force acting on a superparamagnetic bead due to an applied magnetic field," *Lab on a Chip*, vol. 7, no. 10, pp. 1294-1302, July 2007.

[11] J.-B. Mathieu and S. Martel, "Steering of aggregatring magnetic microparticles using propulsion gradient coils in an MRI scanner," *Magnetic Resonance Medicine*, vol. 63, no. 5, pp. 1336-1345, May 2010.

[12] J. D. Keuning, J. de Vries, L. Abelmann, and S. Misra, "Image-based magnetic control of paramagnetic microparticles in water," in *Proceedings of the IEEE International Conference of Robotics and Systems (IROS)*, pp. 421-426, San Francisco, USA, September 2011.

[13] I. S. M. Khalil, J. D. Keuning, L. Abelmann, and S. Misra, "Wireless magnetic-based control of paramagnetic microparticles," in *Proceedings of the IEEE RAS/EMBS International Conference on Biomedical Robotics and Biomechatronics (BioRob)*, pp. 460-466, Rome, Italy, June 2012.

[14] I. S. M. Khalil, R. M. P. Metz, L. Abelmann, and S. Misra, "Interaction force estimation during manipulation of microparticles," in *Proceedings of the IEEE International Conference of Robotics and Systems (IROS)*, pp. 950-956, Vilamoura, Portugal, October 2012.

[15] O. Ergeneman, G. Dogangil, M. P. Kummer, J. J. Abbott, M. K. Nazeeruddin, and B. J. Nelson, "A magnetically controlled wireless optical oxygen sensor for introclular measurements," *IEEE Sensor Journal*, vol. 8, no. 1, pp. 29-37, January 2008.

[16] J. A. Osborn, "Demagnetizing factors of the general ellipsoid," *Physical Review*, vol. 67, no. 11-12, pp. 351-357, June 1945.

[17] D. C. Cronemeyer, "Demagnetizing factors for general ellipsoids," *Journal of Applied Physics*, vol. 70, no. 6, pp. 2911-2914, September 1991.

[18] Z. J. Yang, H. Tsubakihara, S. Kanae, K. Wada, and C. Yi. Su, "A novel robust nonlinear motion controller with disturbance observer," *IEEE Transactions on Control Systems Technology*, vol. 16, no. 1, pp. 137-147, January 2008.

[19] Y. Choi, K. Yang, W. K. Chung, H. R. Kim, and I. H. Suh, "On the robustness and performance of disturbance observers for second-order systems," *IEEE Transactions on Automatic Control*, vol. 48, no. 2, pp. 315-320, February 2003.

[20] S. Katsura, Y. Matsumoto, and K. Ohnishi, "Modeling of force sensing and validation of disturbance observer for force control," *IEEE Transactions on Industrial Electronics*, vol. 54, no. 1, pp. 530-538, February 2007.

[21] J.-B. Mathieu and S. Martel, "Magnetic steering of iron oxide microparticles using proulsion gradient ciols in MRI," in *Proceedings of the International Conference of the IEEE Engineering in Medicine and Biology Society (EMBS)*, pp. 472-475, New York City, USA, September 2006.

[22] T. H. Boyer, "The force on a magnetic dipole," *American Journal of Physics*, vol. 56, no. 8, pp. 688-692, August 1988.

[23] F. Carpi and C. Pappone, "Magnetic maneuvering of endoscopic capsules by means of a robotic navigation system," *IEEE Transactions on Biomedical Engineering*, vol. 56, no. 5, pp. 1482-1490, May 2009.

[24] R. G. McNeil, R. C. Ritter, B. Wang, M. A. Lawson, G. T. Gillies, K. G. Wika, E. G. Quate, M. A. Howard, and M. S. Grady, "Characteristics of an improved magnetic-implant guidance system," *IEEE Transactions on Biomedical Engineering*, vol. 42, no. 8, pp. 802-808, August 1995.

[25] G. L. Shurbet, T. O. Lewis, and T. L. Boullion, "Quadratic matrix equations," *The Ohio Journal of Science*, vol. 74, no. 5, pp. 273-277, September 1974.

[26] S. Komada, N. Machii, and T. Hori, "Control of redundant manipulators considering order of disturbance observer," *IEEE Transactions on Industrial Electronics*, vol. 47, no. 2, pp. 413-420, April 2000.

[27] B. D. Cullity and C. D. Graham, "Introduction to magnetic materials," 2nd ed. *Hoboken, NJ: Wiley*, 2009.

[28] R. Asmatulu, M. A. Zalich, R. O. Claus, and J. S. Riffle, "Synthesis, characterization and targeting of biodegradable magnetic nanocomposite particles by external magnetic fields," *Journal of Magnetism and Magnetic Materials*, Vol. 292, pp. 108-119, November 2005.

[29] S. Martel, O. Felfoul, J.-B. Mathieu, A. Chanu, S. Tamaz, M. Mohammadi, M. Mankiewicz, and N. Tabatabaei, "MRI-based medical nanorobotic platform for the control of magnetic nanoparticles and flagellated bacteria for target interventions in human capillaries," *The International Journal of Robotics Research*, vol. 28, no. 9, pp. 1169-1182, September 2009.